

Droplet formation in a flow focusing configuration: Effects of viscoelasticity

Mohammad Nooranoost, Daulet Izbassarov, and Metin Muradoglu

Citation: [Phys. Fluids](#) **28**, 123102 (2016); doi: 10.1063/1.4971841

View online: <http://dx.doi.org/10.1063/1.4971841>

View Table of Contents: <http://aip.scitation.org/toc/phf/28/12>

Published by the [American Institute of Physics](#)

Articles you may be interested in

[Growth of viscoelastic instabilities around linear cylinder arrays](#)

[Phys. Fluids](#) **28**, 124102 (2016); 10.1063/1.4968221

[Aerodynamics of two-dimensional flapping wings in tandem configuration](#)

[Phys. Fluids](#) **28**, 121901 (2016); 10.1063/1.4971859

[Large-eddy simulations of forced isotropic turbulence with viscoelastic fluids described by the FENE-P model](#)

[Phys. Fluids](#) **28**, 125104 (2016); 10.1063/1.4968218

Droplet formation in a flow focusing configuration: Effects of viscoelasticity

Mohammad Nooranidoost, Daulet Izbassarov, and Metin Muradoglu^{a)}

*Department of Mechanical Engineering, Koç University, Rumelifeneri Yolu,
34450 Sariyer, Istanbul, Turkey*

(Received 22 July 2016; accepted 25 November 2016; published online 16 December 2016)

We numerically investigate the effects of bulk fluid viscoelasticity on droplet formation and dynamics in an axisymmetric flow focusing configuration. Viscoelasticity is modeled using the finitely extensible nonlinear elastic-Chilcott-Rallison (FENE-CR) model. Extensive simulations are performed to examine droplet formation and breakup dynamics for a wide range of parameters including flow rate ratio, Weissenberg number, polymeric viscosity ratio, and extensibility parameter. It is found that these parameters have a significant influence on the droplet size and size distribution (dispersity). Three different regimes are observed in the sequence of squeezing, dripping, and jetting modes as the flow rate ratio is increased. It is also found that the viscoelasticity has a similar effect as decreasing flow rate ratio and acts to delay transition from squeezing to dripping and from dripping to jetting regimes. The strain-rate hardening occurs at a critical Weissenberg number resulting in an abrupt increase in droplet size and this effect is more pronounced as the polymeric viscosity ratio is increased. *Published by AIP Publishing.* [<http://dx.doi.org/10.1063/1.4971841>]

I. INTRODUCTION

Flow focusing devices are widely used in microfluidics to generate droplets with precisely controlled size and dispersity. Formation of monodispersed droplets finds applications in a wide range of areas such as chemical engineering,¹ biotechnology,² and drug delivery systems.³ Very often, these applications involve complex fluids exhibiting a viscoelastic behavior. Viscoelastic liquids demonstrate various exotic behaviors like die-swell, Weissenberg, and tubeless siphon effects.⁴ These complicated rheological behaviors have been exploited in microfluidic applications such as a microfluidic memory and control device,⁵ a microfluidic rectifier,⁶ a nonlinear viscoelastic flow resistor,⁵ synthesis of non-spherical particles,⁷ and enhanced mixing.⁸ All these functionalities rely on viscoelasticity of working fluids. Therefore, understanding the rheological behavior of viscoelastic fluids is of both fundamental and practical importance.⁹

Formation of Newtonian droplets in another Newtonian medium (NN system) has been extensively studied both experimentally^{10–14} and numerically.^{15–17} However, effects of viscoelasticity on droplet formation have received less attention. In particular, effects of viscoelasticity in a flow focusing geometry have been subject of a few experimental^{18,19} and numerical^{15,20} studies.

Droplet formation in two-phase viscoelastic systems has been often investigated experimentally. The early studies considered the formation of viscoelastic droplets in a Newtonian medium (VN system). Husny and Cooper-White²¹ found that the presence of elasticity produces elongated filaments in T-shaped microchannels resulting in the formation of secondary droplets. The number and polydispersity of these droplets were found to be dependent on the viscosity ratio of the phases. Steinhilber *et al.*¹⁸ studied the effects of fluid elasticity and channel dimensions on droplet formation in a flow focusing device. Their results show that higher molecular weight of polymers brings about larger extensional viscosity, longer thread, and longer pinch-off time. Arratia *et al.*²² conducted extensive experiments to investigate the effects of polymer molecular weight on filament thinning

^{a)} Author to whom correspondence should be addressed. Electronic mail: mmuradoglu@ku.edu.tr

and droplet formation in a cross-slot microchannel. They observed that the liquid filament becomes longer and breakup time increases as the molecular weight is increased. They also found that extensional viscosity decreases non-monotonically with decreasing molecular weight. Later, Lee *et al.*¹⁹ investigated competition between viscoelasticity and surfactant dynamics in a flow focusing device. They identified a region in the parameter space where the viscoelasticity couples with the surfactant dynamics to form a long thread before the breakup. They suggested that the synergy between these two properties can be used as a tool to manipulate droplet formation in these devices. Recently, Li *et al.*²³ studied the dynamics of viscoelastic droplets under very low interfacial tension in a T-junction device. They found that an unstable tail fragmentation occurs at the rear of the droplet after a critical value of Weissenberg number and this phenomenon can be controlled by adjusting flow rate ratios and viscoelasticity.

In recent years, the formation of Newtonian droplets in a viscoelastic medium (NV system) has received more attention. Derzsi *et al.*²⁴ experimentally investigated the effects of viscoelasticity on droplet formation in various cross slot and flow focusing geometries. They found that the viscoelasticity can lower polydispersity of emulsions and reduce droplet size by careful adjustment of the viscosity ratio. Chiarello *et al.*²⁵ compared the formation of oil drops in Newtonian and shear-thinning fluids in a T-junction device. Their experiments showed a negligible difference between these two systems. Fu *et al.*²⁶ also conducted an experimental study on T-shaped microchannels and found that the concentration of polymers and the size of a microfluidic device are the two important factors influencing the flow regime. More recently, Fu *et al.*²⁷ investigated breakup dynamics of silicone oil droplets in a shear thinning fluid using a flow focusing geometry. They studied and characterized different stages of the breakup process and found that the breakup process can be divided into a non-universal collapse stage followed by a universal fast pinch-off stage.

The effects of viscoelasticity have been also studied computationally using various viscoelastic fluid models and numerical approaches. The viscoelastic multiphase systems exhibit very rich dynamics mainly due to the strong interactions between viscoelasticity and interfaces and thus pose a challenging problem for computational fluid dynamics. Strong nonlinear interactions between viscoelasticity, fluid-fluid interface, and channel walls make the problem even more difficult in microchannels. In addition, the Weissenberg number is usually high in microfluidic applications due to small length scales and high deformation rates, which makes the viscoelastic model equations stiff and thus more difficult to solve numerically. The early numerical study was performed by Zhou *et al.*¹⁵ They used a diffuse-interface method and performed extensive simulations mainly to examine the Newtonian droplet formation in another Newtonian fluid (NN system) in an axisymmetric flow focusing geometry. As a part of this investigation, they also performed a few simulations to examine the effects of viscoelasticity contained in the droplet phase (VN system) using the Oldroyd-B model. They concluded that the viscoelasticity suppresses the formation of satellite droplets and may increase or decrease the final droplet size depending on the flow regime. They also found that the viscoelasticity in the droplet phase increases/decreases the droplet size in a dripping/jetting regime. Recently, Gupta and Sbragaglia^{20,28} performed comprehensive three dimensional simulations in both planar T-junction and flow focusing geometries using a lattice Boltzmann method. The viscoelasticity was modeled using the finite extensible nonlinear elastic dumbbells with the closure proposed by Peterlin (FENE-P model).^{29,30} They considered both the NV and the VN systems and found that the effects of viscoelasticity in the continuous phase are more pronounced than those in the dispersed phase for both geometries. They also found that increasing viscoelasticity of outer phase decreases droplet size and filament length and shifts the breakup location closer to the junction.

In the present study, we numerically examine the effects of viscoelasticity contained in the bulk fluid on droplet formation and breakup dynamics in an axisymmetric flow focusing configuration. The numerical method is based on the finite-difference/front-tracking algorithm developed by Izbassarov and Muradoglu.³¹ The viscoelasticity is accounted for using the finitely extensible nonlinear elastic-Chilcott-Rallison (FENE-CR) model.³² Extensive simulations are performed to investigate droplet formation for a wide range of parameters including flow rate ratio (Γ), Weissenberg number (Wi), polymeric viscosity ratio (β), and extensibility parameter (L) in the range of $1 \leq \Gamma \leq 8$, $0 \leq Wi \leq 100$, $0 \leq \beta \leq 0.8$, and $5 \leq L < \infty$.

II. FORMULATION AND NUMERICAL METHOD

The governing equations are briefly described in the framework of the finite-difference/front-tracking method.³³ The flow is assumed to be incompressible. Following the work of Tryggvason *et al.*³⁴ and Izbassarov and Muradoglu,³¹ a one-field formulation is used in which a single set of governing equations is solved in the entire computational domain including the dispersed and the continuous phases. The effects of surface tension are fully accounted through the body forces distributed near the interface. In this formulation, the continuity and momentum equations can be written as

$$\nabla \cdot \mathbf{u} = 0, \quad (1)$$

$$\frac{\partial \rho \mathbf{u}}{\partial t} + \nabla \cdot (\rho \mathbf{u} \mathbf{u}) = -\nabla p + \nabla \cdot \mu_s (\nabla \mathbf{u} + \nabla \mathbf{u}^T) + \nabla \cdot \boldsymbol{\tau} + \int_A \gamma \kappa \mathbf{n} \delta(\mathbf{x} - \mathbf{x}_f) dA, \quad (2)$$

where μ_s , ρ , p , \mathbf{u} , and $\boldsymbol{\tau}$ denote the solvent viscosity, the density, the pressure, the velocity vector, and the viscoelastic extra stress tensor, respectively. The last term in Eq. (2) represents the body force due to surface tension where γ is the surface tension coefficient, κ is twice the mean curvature, and \mathbf{n} is the unit vector normal to the interface. The surface tension acts only on the interface as indicated by the three-dimensional delta function, δ , whose arguments \mathbf{x} and \mathbf{x}_f are the points at which the equation is being evaluated and a point at the interface, respectively.

The FENE-CR model is adopted as the constitutive equation for the viscoelastic extra stresses. This model can be written as

$$\frac{\partial \mathbf{A}}{\partial t} + \nabla \cdot (\mathbf{u} \mathbf{A}) - (\nabla \mathbf{u})^T \cdot \mathbf{A} - \mathbf{A} \cdot \nabla \mathbf{u} = -\frac{F_A}{\lambda} (\mathbf{A} - \mathbf{I}),$$

$$F_A = \frac{L^2}{L^2 - \text{trace}(\mathbf{A})}, \quad (3)$$

where \mathbf{A} , λ , L , F_A , and \mathbf{I} are the conformation tensor, the relaxation time, the extensibility parameter defined as the ratio of the length of a fully extended polymer dumbbell to its equilibrium length, the stretch function, and the identity tensor, respectively. The extra stress tensor $\boldsymbol{\tau}$ is related to the conformation tensor as

$$\boldsymbol{\tau} = \frac{F_A \mu_p}{\lambda} (\mathbf{A} - \mathbf{I}), \quad (4)$$

where μ_p is the polymeric viscosity.

It is also assumed that the material properties remain constant following a fluid particle, i.e.,

$$\frac{D\rho}{Dt} = 0, \frac{D\mu_s}{Dt} = 0, \frac{D\mu_p}{Dt} = 0, \frac{D\lambda}{Dt} = 0, \quad (5)$$

where $\frac{D}{Dt} = \frac{\partial}{\partial t} + \mathbf{u} \cdot \nabla$ is the material derivative. The density, polymeric and solvent viscosities, and the relaxation time vary discontinuously across the fluid interface and are given by

$$\mu_p = \mu_{p,i} \phi + \mu_{p,o} (1 - \phi), \quad \mu_s = \mu_{s,i} \phi + \mu_{s,o} (1 - \phi),$$

$$\rho = \rho_i \phi + \rho_o (1 - \phi), \quad \lambda = \lambda_i \phi + \lambda_o (1 - \phi), \quad (6)$$

where the subscripts i and o denote the properties of the droplet and the bulk fluids, respectively. In Eq. (6), ϕ is the indicator function defined such that it is unity inside the droplet and zero outside.

The flow equations (Eqs. (1)–(2)) are solved fully coupled with the viscoelastic model equations (Eq. (3)) by the finite-difference/front-tracking method developed by Izbassarov and Muradoglu.³¹ The front-tracking method has proven to be a viable tool for the simulation of viscoelastic interfacial flow systems.^{31,35,36} A complete description of the front-tracking method and the treatment of the viscoelasticity can be found in the works of Tryggvason *et al.*³⁴ and Izbassarov and Muradoglu,³¹ respectively.

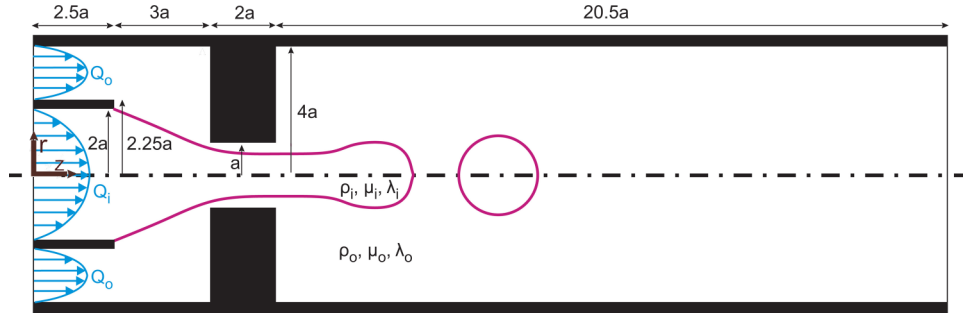


FIG. 1. Schematic illustration of the flow focusing geometry.

III. PROBLEM STATEMENT

The physical problem and computational domain are sketched in Fig. 1. The flow is assumed to be axisymmetric. Therefore, only one half is used as the computational domain. The outer tube contains a short concentric pipe at the inlet and a 4:1:4 contraction/expansion section in the further downstream. The radii of the inner and the outer pipes, and the contraction are $2a$, $4a$, and a , respectively. The total length of the tube is $28a$. The thickness and the length of the inner pipe are $0.25a$ and $2.5a$, respectively. A sudden contraction of width $2a$ is located at $5.5a$ from the inlet as shown in Fig. 1. The interface is initially flat at the exit of the inner pipe. The flow is initiated instantaneously by imposing fully developed velocity profiles in the inner pipe and the annulus.³⁷ At the inlet, the flow rates are fixed and denoted by Q_i and Q_o in the inner pipe and the annulus, respectively. The flow rate ratio is then defined as $\Gamma = Q_o/Q_i$. The pressure is fixed at the outlet. Symmetry and no-slip boundary conditions are used at the centerline and on the wall of the tubes, respectively. The viscoelastic stress tensor is specified at the inlet based on the analytical solution assuming a fully developed flow.³¹ The Neumann boundary conditions are used for all viscoelastic stress components at the other boundaries.

The governing equations are solved in their dimensional forms but the results are expressed in terms of relevant non-dimensional quantities. The average velocity in the annulus $\mathcal{U} = Q_o/A_o$, where A_o is the cross-sectional area of the annulus, is used as the velocity scale. The radius of the orifice is used as the length scale ($\mathcal{L} = a$). Thus the time scale is defined as $\mathcal{T} = aA_o/Q_o$. In addition to the extensibility parameter (L), the other governing non-dimensional numbers are then defined as

$$Wi = \frac{\lambda \mathcal{U}}{a}, Ca = \frac{\mu_o \mathcal{U}}{\gamma}, Re = \frac{\rho_o \mathcal{U} a}{\mu_o}, \Gamma = \frac{Q_o}{Q_i}, \alpha = \frac{\rho_o}{\rho_i}, \theta = \frac{\mu_o}{\mu_i}, \beta = \frac{\mu_p}{\mu_p + \mu_s}, \quad (7)$$

where Wi , Ca , and Re are the Weissenberg, the capillary, and the Reynolds numbers, respectively. The other parameters α , θ , and β denote the density, total, and polymeric viscosity ratios, respectively. Density and total viscosity ratios are fixed at the values of $\alpha = 1$ and $\theta = 2$ in all the results presented in this paper. Simulations are then performed by varying only one parameter while keeping all the other constants in order to demonstrate the sole effects of the parameter on flow. To facilitate this, we define a base case as $Wi = 1$, $Re = 0.75$, $Ca = 1.5 \times 10^{-3}$, $\Gamma = 2$, $\beta = 0.5$, and $L = 5$. The base case is determined to be representative of the experimental values used by Derzsi *et al.*²⁴

IV. RESULTS AND DISCUSSIONS

Extensive simulations are performed to study the effects of viscoelasticity on droplet generation in the flow focusing configuration. In particular, the effects of the flow rate ratio, the Weissenberg number, the polymeric viscosity ratio, and the extensibility parameter are investigated. A uniform Cartesian grid is employed in the computations. A grid convergence study is done to determine the minimum grid size required to reduce the spatial discretization error below a threshold value. As

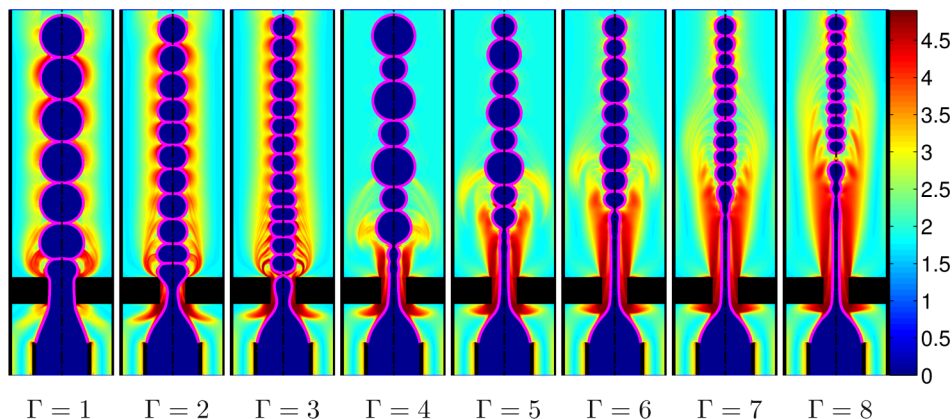


FIG. 2. Effects of flow rate ratio (Γ) on formation of Newtonian droplets in a viscoelastic ambient fluid. The contours represent the average polymer extension $\sqrt{\text{trace}(\mathbf{A})}$. The droplet formation patterns are shown for the range of $1 \leq \Gamma \leq 8$ corresponding to $7.5 \times 10^{-4} \leq Ca \leq 6 \times 10^{-3}$ and $0.375 \leq Re \leq 3$. The other parameters are $Wi = 1$, $\beta = 0.5$, and $L = 5$.

detailed in the [supplementary material](#), it is found that a computational grid containing 128×896 cells in the radial and axial directions, respectively, is sufficient to reduce the spatial error below 2% for all the flow quantities. Therefore this grid resolution is used in all the results presented in this paper unless specified otherwise.

First, the effects of the flow rate ratio (Γ) are investigated. For this purpose, we performed simulations for various flow rate ratios in the range of $1 \leq \Gamma \leq 8$. Note that the inner flow rate is fixed and the outer flow rate is changed to alter the flow rate ratio. The relaxation time is adjusted to keep the Weissenberg number constant for different flow rate ratios. The square root of the trace of conformation tensor ($\sqrt{\text{trace}(\mathbf{A})}$) is also used as a measure of average polymer extension. The droplet formation patterns are shown in Fig. 2 for various flow rate ratios. As can be seen in this figure, droplet formation occurs in three main regimes: squeezing ($\Gamma \leq 1$), dripping ($\Gamma = 2 - 3$), and jetting ($\Gamma \geq 4$). These regimes are qualitatively similar to those observed for all Newtonian systems (NN).¹⁴ In the squeezing regime, a low amount of outer flow passing through the orifice allows the inner flow to easily occupy the entire cross section of the orifice resulting in the formation of thick filament and thus large droplets. Viscoelastic stresses are mainly generated around the orifice region and convected further downstream as seen in Fig. 2. As Γ increases, droplet formation shifts to the dripping regime in which the breakup process starts to be significantly influenced by the shear forces of the outer fluid resulting in the formation of a thinner filament and smaller droplets. Similar to the squeezing regime, the viscoelastic stresses accentuate in the vicinity of the orifice and around the filament. The breakup occurs just at the exit of the orifice in both squeezing and dripping regimes. After the breakup, the tip of the liquid filament becomes sharp and retracts back leaving the orifice completely in the squeezing regime. As the flow rate ratio is increased from $\Gamma = 3$ to $\Gamma = 4$, a transition occurs from the dripping to the jetting regime with a dramatic increase in droplet size. In addition, the droplets become polydispersed. In this regime, breakup mechanism is mainly driven by the Rayleigh-Plateau instability but gets highly complicated due to strong interactions of interface with the viscoelastic co-flowing fluid stream and confinement. After formation of the main large droplet, the remaining liquid filament has a sharp edge which rapidly retracts backward creating a bulb at the tip and eventually leads to the formation of a secondary smaller droplet. This is qualitatively similar to the experimental observations of Derzsi *et al.*²⁴ except for that they also observed a few satellite droplets that are much smaller than the secondary droplet. Note that the size of satellite droplets observed by Derzsi *et al.*²⁴ is much smaller than our grid resolution, which is most likely the reason why we do not observe them in the present simulations. By further increasing Γ , the jetting regime occurs in which the filament becomes longer before it breaks up into droplets in the further downstream of the orifice. In this regime, the viscoelastic stresses built up in the orifice and around the filament in the downstream of the orifice due to extreme stretching of polymers. It is also observed that droplets become less polydispersed as Γ increases.

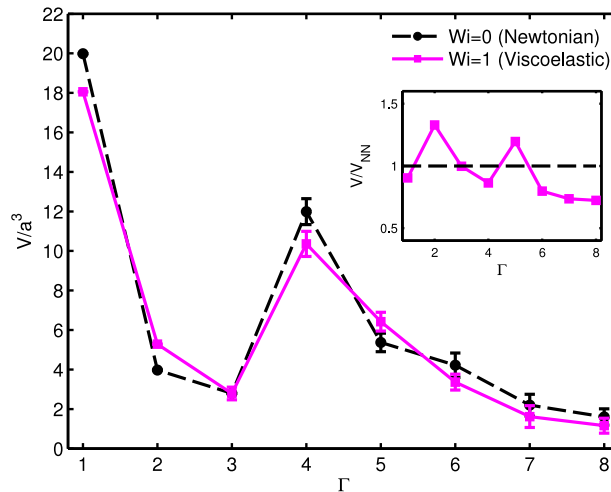


FIG. 3. Effects of flow rate ratio (Γ) on droplet size in both the NN and NV systems. The droplet size is normalized by $V_{ref} = a^3$. The error bars represent the coefficient of variation of droplet size indicating the polydispersity. In the inset, the droplet size is normalized by that obtained for the corresponding NN system. Normalized droplet size is plotted for the range of $1 \leq \Gamma \leq 8$ corresponding to $7.5 \times 10^{-4} \leq Ca \leq 6 \times 10^{-3}$ and $0.375 \leq Re \leq 3$. The other parameters are $\beta = 0.5$ and $L = 5$.

Next, the effects of flow rate ratio on droplet size are quantified. We take average volume of droplets as a measure of droplet size (V) and normalize it by the reference volume defined as $V_{ref} = a^3$. Note that first few droplets are usually much larger than the average droplet size obtained in the steady state. Therefore we disregarded first eight droplets in computing average droplet size and its variance. Normalized droplet size for both the NN and NV systems is plotted against the flow rate ratio in Fig. 3 for $Wi = 0$ (Newtonian) and $Wi = 1$ (viscoelastic) cases. The error bars represent the coefficient of variation defined as $CV(\%) = 100 \times \sigma/V$, where σ is the standard deviation of droplet size and is used as a measure of polydispersity. Note that the error bars are not shown and the droplets are assumed to be uniform in the case of small coefficient of variation, i.e., $CV \leq 5\%$. It is observed that in both the NN and NV systems, droplet size usually decreases with Γ except for the transition between the dripping and the jetting regimes, where droplet size increases abruptly and droplets become highly polydispersed. The trends for both the NN and NV systems are similar, which is consistent with the experimental observations of Derzsi *et al.*²⁴ It is also observed that polydispersed droplets are mainly produced in the jetting regime. The polydispersity increases in the transition from the dripping to the jetting regime and slightly decreases as the flow rate ratio is further increased in the jetting regime. The inset of Fig. 3 shows the average droplet size obtained in the viscoelastic system (solid line) normalized by the corresponding droplet size in the all Newtonian system (dashed line). The error bars are not shown in the inset for the sake of clarity. As can be seen in the inset, the effects of the viscoelasticity on the droplet size are non-monotonic and depend on the flow rate ratio. It is also seen that the viscoelasticity increases droplet size in the dripping regime but decreases it in the jetting regime with a transition in between. Note that similar observations were also made by Zhou *et al.*¹⁵ for the VN system.

We next examine the effects of the Weissenberg number on droplet formation. Simulations are performed for the range of $0.1 \leq Wi \leq 100$ and for the flow rate ratios of $\Gamma = 1, 2, 4$, and 8 . The droplet formation patterns are plotted in Fig. 4 where the constant contours of the average polymer extension ($\sqrt{\text{trace}(\mathbf{A})}$) are also shown. For the case of $Wi = 0.1$, the polymer stretching is mainly confined in the vicinity of the orifice with little influence on droplet dynamics. As Wi increases, the viscoelastic stresses expand further downstream and eventually cover the entire cross section of the channel. The Weissenberg number does not have large effects on the average droplet size and size distribution except for the case of $\Gamma = 4$ in which the droplet formation occurs in the jetting regime at low Wi and shifts to the dripping regime as Wi increases. In the case of $\Gamma = 4$, the droplets are large and monodispersed at low Wi ($Wi < 1$), get polydispersed at moderate $Wi = O(1)$, and become uniform with a smaller size for $Wi \geq 10$. In the jetting regime, as Wi increases, highly

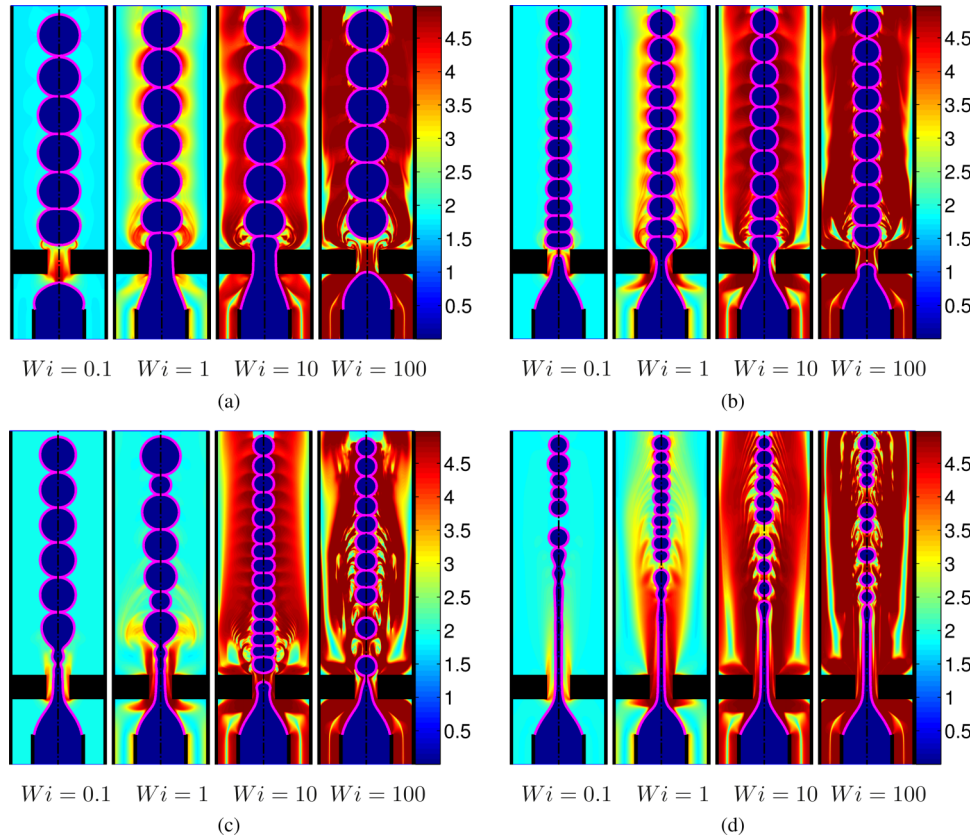


FIG. 4. Effects of Weissenberg number on droplet formation for different flow rate ratios. The contours represent the average polymer extension $\sqrt{\text{trace}(\mathbf{A})}$. For $\Gamma = 1, 2, 4, 8$, the corresponding capillary and Reynolds numbers are $Ca = 7.5 \times 10^{-4}, 1.5 \times 10^{-3}, 3 \times 10^{-3}, 6 \times 10^{-3}$ and $Re = 0.375, 0.75, 1.5, 3$, respectively. The other parameters are $\beta = 0.5$ and $L = 5$. (a) $\Gamma = 1$. (b) $\Gamma = 2$. (c) $\Gamma = 4$. (d) $\Gamma = 8$.

stretched polymers induce high extensional viscosity in the contraction region, which reduces the filament length and moves the breakup point closer to the orifice. These results are consistent with the findings of Gupta and Sbragaglia.²⁰ Due to the finitely extensible nature of the FENE-CR model, a further increase in Wi number results in only a minor change in the flow field for $Wi \geq 10$ as seen in Fig. 4(d). The effects of Wi are quantified in Fig. 5 where the average droplet size and size distribution are plotted against Wi for different flow rate ratios. As seen, the average droplet size and size distribution are most sensitive to Wi for $\Gamma = 4$. For this case, the average droplet size gets significantly smaller as Wi increases.

In a typical experimental study, the fluid viscoelasticity is usually increased by adding more polymers into the solvent increasing both the polymeric viscosity and the relaxation time. To mimic this, further simulations are performed to examine the combined effects of Weissenberg number (Wi) and the polymeric viscosity ratio (β) in the range of $0 \leq Wi \leq 100$ and $0 \leq \beta \leq 0.8$ while keeping all other parameters fixed at their values in the base case. Figure 6 shows the variation of droplet size and size distribution as a function of Wi for the polymeric viscosity ratios of $\beta = 0, 0.2, 0.5$, and 0.8 . As seen, the viscoelasticity does not have a significant influence on the droplet size until a critical Weissenberg number (Wi_{cr}) is reached, i.e., $Wi \lesssim Wi_{cr}$. When the Weissenberg number exceeds the critical value, the droplet size increases abruptly reaching another nearly constant value. The critical Weissenberg number weakly depends on the polymeric viscosity ratio and varies in the range of $0.6 \lesssim Wi_{cr} \lesssim 1$ for $0.2 \leq \beta \leq 0.8$ in the present case. The critical Weissenberg number slightly decreases as the polymeric viscosity ratio increases, which is consistent with the experimental observations of Arratia *et al.*²² The polymeric viscosity ratio has a negligible influence on the droplet size when $Wi < Wi_{cr}$ but the droplet size increases rapidly with

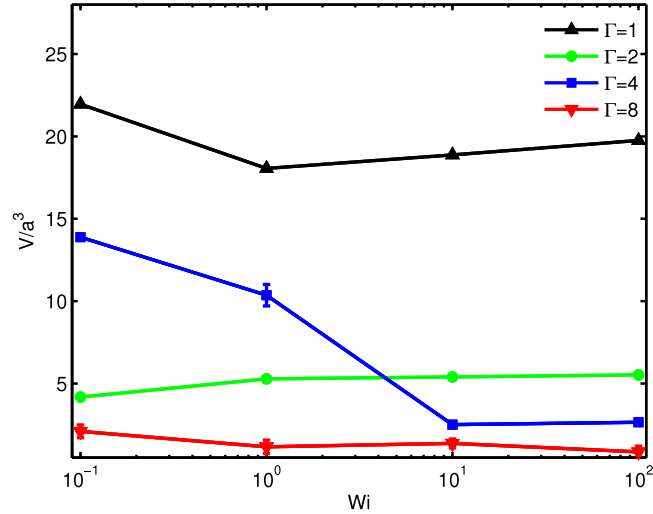


FIG. 5. Effects of Weissenberg number on droplet size for different flow rate ratios. The droplet size is normalized by $V_{ref} = a^3$. The error bars represent the coefficient of variation of droplet size indicating the polydispersity. For $\Gamma = 1, 2, 4, 8$, the corresponding capillary and Reynolds numbers are $Ca = 7.5 \times 10^{-4}, 1.5 \times 10^{-3}, 3 \times 10^{-3}, 6 \times 10^{-3}$ and $Re = 0.375, 0.75, 1.5, 3$, respectively. The other parameters are $\beta = 0.5$ and $L = 5$.

β after $Wi > Wi_{cr}$. We attribute this sudden increase in droplet size to the well known strain-rate hardening effects of polymeric fluids.^{22,38–40} As discussed by Arratia *et al.*,²² rapid stretching of polymer molecules results in a sharp increase in the extensional viscosity of polymeric fluids and this phenomenon is known as the strain-rate hardening. Tamaddon-Jahromi *et al.*⁴⁰ demonstrated that the FENE-CR model qualitatively captures the main features of the strain-rate hardening behavior. For the FENE-CR model, the steady extensional viscosity (μ_e) can be expressed for a uniaxial extensional flow as⁴⁰

$$\mu_e = 3\mu_s + 3\mu_p \left[\frac{F_A}{F_A^2 - F_A Wi - 2Wi^2} \right]. \quad (8)$$

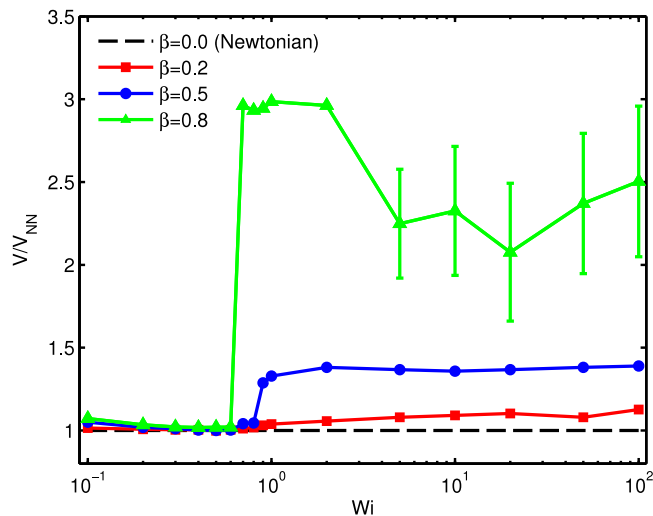


FIG. 6. Combined effects of the Weissenberg number and the polymeric viscosity ratio on the average droplet size and size distribution in the range of $0 \leq Wi \leq 100$ and $0 \leq \beta \leq 0.8$. The average droplet size in the NV system is normalized by that obtained for the corresponding NN case ($V_{NN} \approx 3.97a^3$). The error bars represent the coefficient of variation of droplet size indicating the polydispersity. The other parameters are $Re = 0.75$, $Ca = 1.5 \times 10^{-3}$, $\Gamma = 2$, and $L = 5$.

Tamaddon-Jahromi *et al.*⁴⁰ showed that the extensional viscosity grows sharply around $Wi_{cr} = 0.7$ which is in good agreement with the present results shown in Fig. 6. In the present configuration, the elongational viscosity increases rapidly due to stretching of polymers in the vicinity of the orifice resulting in large resistance to stretching of liquid filament. Once the polymers are fully stretched, the extensional viscosity becomes independent of the Weissenberg number, which may explain the nearly constant droplet size after $Wi > Wi_{cr}$ as seen in Fig. 6. It is interesting to see that the droplets become highly polydispersed for the case of very large polymeric viscosity ratios and large Weissenberg numbers (i.e., $\beta \geq 0.8$ and $Wi > 5$) as indicated by the error bars in Fig. 6.

Further simulations are performed to examine the breakup process around the critical Weissenberg number. The polymeric viscosity ratio is set to be $\beta = 0.8$ to enhance the effects of the viscoelasticity on the droplet formation. The droplet breakup processes for $Wi = 0.6$ and $Wi = 0.7$ are depicted in Fig. 7 where the enlarged snapshots are shown in the vicinity of the orifice at various times. The mode of breakup is determined by the competition between the viscoelastic and viscous effects. In the case of $Wi = 0.6$, the viscous effects are still dominant over the viscoelasticity, and thus the breakup occurs in the dripping regime. On the other hand, the extensional viscosity increases rapidly as Wi increases from 0.6 to 0.7 due to the strain-rate hardening effects and makes the liquid filament to fully obstruct the entire cross section of the orifice. As a result, the breakup occurs in the squeezing regime producing larger droplets as seen in Fig. 7(b).

Finally, the effects of the extensibility parameter (L) are examined by varying the extensibility parameter in the range of $5 \leq L < \infty$ while keeping the other parameters the same as the base case. Note that the Oldroyd-B fluid model is used for the case of $L \rightarrow \infty$. The droplet formation patterns are shown in Fig. 8 where the constant contours of the average polymer extension ($\sqrt{\text{trace}(\mathbf{A})}$) are also plotted to demonstrate the evolution of viscoelastic stresses. The effects of

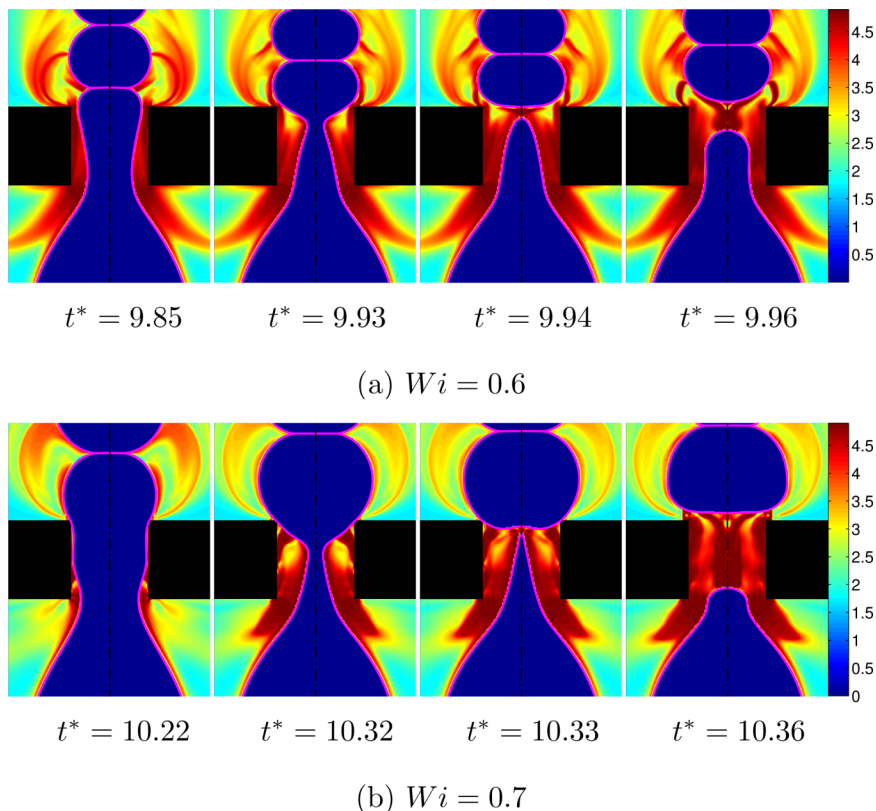


FIG. 7. Droplet formation process in the vicinity of the orifice computed for (a) $Wi = 0.6$ (dripping) and (b) $Wi = 0.7$ (squeezing). The contours represent the average polymer extension $\sqrt{\text{trace}(\mathbf{A})}$. The other parameters are $Re = 0.75$, $Ca = 1.5 \times 10^{-3}$, $\Gamma = 2$, $\beta = 0.8$, and $L = 5$.

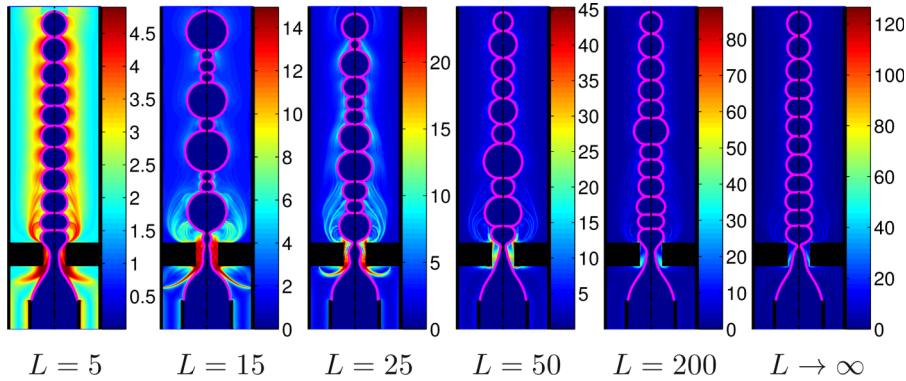


FIG. 8. Effects of the extensibility parameter (L) on droplet formation. The contours represent the average polymer extension $\sqrt{\text{trace}(\mathbf{A})}$. The other parameters are $Wi = 1$, $Re = 0.75$, $Ca = 1.5 \times 10^{-3}$, $\Gamma = 2$, and $\beta = 0.5$.

the extensibility parameter are also quantified in Fig. 9 where the average droplet size is plotted against L . As mentioned before, the error bars indicate the variation of droplet size or polydispersity in Fig. 9. As seen in Figs. 8 and 9, the extensibility parameter has a non-monotonic effect on the average droplet size and size distribution. Viscoelasticity generally increases the droplet size and polydispersity compared to the corresponding all Newtonian system as seen in Fig. 9. Highly monodispersed droplets are generated at low values of the extensibility parameter ($L \leq 5$). As L is increased, the monodispersity is first lost and then partly recovered resulting in highly polydispersed and nearly uniform droplets for $5 < L \leq 200$ and $L \rightarrow \infty$, respectively. At low L , all the polymers are fully stretched to their maximum extensibility resulting in nearly uniform viscoelastic stresses in the orifice region. Thus the viscoelasticity essentially increases the effective extensional viscosity uniformly in the orifice. As L is increased to the moderate values, the viscoelastic stresses become more non-uniform and complex making the breakup process highly irregular and unpredictable. Further increase in L confines viscoelastic stresses in a thin boundary layer near the orifice wall. As a result, the viscoelastic effects on the droplet breakup process are reduced making the droplets again more monodispersed. For example, in the case of $L = 15$ in Fig. 8, the viscoelastic stresses are nearly uniform in the constriction region, which acts to stabilize the liquid filament and results

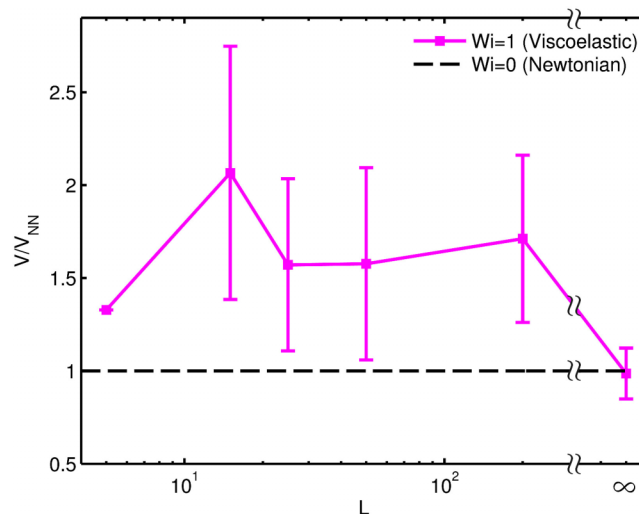


FIG. 9. Effects of the extensibility parameter (L) on the average droplet size normalized by that obtained for the corresponding NN case ($V_{NN} \approx 3.97a^3$). The error bars represent the coefficient of variation of droplet size indicating the polydispersity. The other parameters are $Re = 0.75$, $Ca = 1.5 \times 10^{-3}$, $\Gamma = 2$, and $\beta = 0.5$.

in a larger main droplet compared to the corresponding all Newtonian case. After the creation of the main large droplet, the tip of the interface retracts rapidly towards the inlet of the constriction and significantly perturbs the viscoelastic boundary layer on the wall of the constriction. Until the viscoelastic boundary layer is restored, a few much smaller droplets are generated. This process repeats as seen in Fig. 8. For larger L values, e.g., $L = 25$, the mechanism is very similar but the restoring time gets shorter as L increases. Therefore the size of the secondary droplets gets larger as L increases and eventually the droplet production becomes monodispersed. Although not shown here, simulations are also performed and a very similar trend is observed for the case of $Wi = 100$.

V. CONCLUSIONS

The effects of viscoelasticity are examined numerically for droplet formation in an axisymmetric flow focusing configuration. The viscoelasticity is contained only in the continuous phase and comprehensive simulations are performed for a wide range of flow parameters including flow rate ratio (Γ), the Weissenberg number (Wi), the polymeric viscosity ratio (β), and the extensibility parameter (L). Squeezing, dripping, and jetting regimes are identified depending on the non-dimensional parameters.

We found that the droplet formation occurs in the squeezing regime at low flow rate ratios in which the liquid filament occupies the entire orifice cross section and breakup occurs at the exit of the orifice. As the flow rate ratio increases, the liquid filament gets thinner and breakup occurs in the dripping mode at the exit of the orifice. Further increase in the flow rate ratio shifts breakup mode from the dripping to the jetting regime in which a long thread forms in the expansion region before the breakup takes place. These three breakup modes are very similar to the all Newtonian case but the viscoelasticity delays transition from the squeezing to the dripping and from the dripping to the jetting regimes. The average droplet size generally decreases as the flow rate ratio increases except for the transition from the dripping to the jetting regime in which both average droplet size and polydispersity increase.

Viscoelasticity influences the average droplet size and size distribution in a complicated way depending on the working conditions. It is found that increasing Weissenberg number has a similar effect as decreasing the flow rate ratio mainly due to the strain-rate hardening effect of viscoelasticity. The average droplet size and size distribution are found to be the most sensitive to Wi in the dripping regime. In this regime, an abrupt increase in the average droplet size occurs at a critical Weissenberg number at which droplet formation shifts from the dripping to the squeezing regime. This effect is more pronounced at higher polymeric viscosity ratios. The critical Weissenberg number is found to weakly depend on the polymeric viscosity ratio and be closely related to the critical strain rate at which the “strain-rate hardening” occurs. The average droplet size and size distribution remain nearly constant after the critical Weissenberg number except for the case of very high polymeric viscosity ratio in which the average droplet size decreases while polydispersity increases at high Weissenberg numbers, i.e., about $Wi > 5$.

We also found that the extensibility parameter influences the droplet size and size distribution non-monotonically in the dripping regime. Highly monodispersed droplets are generated at low values of the extensibility parameter. As the extensibility parameter is increased, the monodispersity is first lost and then partly recovered resulting in highly polydispersed and then nearly uniform droplets for $5 < L \leq 200$ and $L \rightarrow \infty$, respectively.

SUPPLEMENTARY MATERIAL

See [supplementary material](#) for the grid convergence study.

ACKNOWLEDGMENTS

The authors are grateful to the Scientific and Technical Research Council of Turkey (TUBITAK) for the support of this research through Grant No. 112M181 and Turkish Academy of Sciences

(TUBA). The authors are grateful for the use of the computing facilities at TUBITAK-ULAKBIM, High Performance and Grid Computing Center.

- ¹ O. A. Basaran, "Small-scale free surface flows with breakup: Drop formation and emerging applications," *AIChE J.* **48**(9), 1842–1848 (2002).
- ² A. D. Griffiths and D. S. Tawfik, "Miniaturising the laboratory in emulsion droplets," *Trends Biotechnol.* **24**(9), 395–402 (2006).
- ³ C.-X. Zhao, "Multiphase flow microfluidics for the production of single or multiple emulsions for drug delivery," *Adv. Drug Delivery Rev.* **65**(11), 1420–1446 (2013).
- ⁴ R. B. Bird, *Dynamics of Polymeric Liquids* (Wiley, New York, 1977), ISBN: 047107375 0471015962.
- ⁵ A. Groisman, M. Enzelberger, and S. R. Quake, "Microfluidic memory and control devices," *Science* **300**(5621), 955–958 (2003).
- ⁶ A. Groisman and S. R. Quake, "A microfluidic rectifier: Anisotropic flow resistance at low Reynolds numbers," *Phys. Rev. Lett.* **92**(9), 094501 (2004).
- ⁷ D. Dendukuri, K. Tsoi, T. A. Hatton, and P. S. Doyle, "Controlled synthesis of nonspherical microparticles using microfluidics," *Langmuir* **21**(6), 2113–2116 (2005).
- ⁸ A. Groisman and V. Steinberg, "Efficient mixing at low Reynolds numbers using polymer additives," *Nature* **410**(6831), 905–908 (2001).
- ⁹ M. S. N. Oliveira, M. A. Alves, and F. T. Pinho, "Microfluidic flows of viscoelastic fluids," in *Transport and Mixing in Laminar Flows: From Microfluidics to Oceanic Currents* (Wiley-VCH Verlag GmbH & Co. KGaA, Weinheim, Germany, 2011), pp. 131–174.
- ¹⁰ P. Garstecki, I. Gitlin, W. DiLuzio, G. M. Whitesides, E. Kumacheva, and H. A. Stone, "Formation of monodisperse bubbles in a microfluidic flow-focusing device," *Appl. Phys. Lett.* **85**(13), 2649–2651 (2004).
- ¹¹ P. Garstecki, M. J. Fuerstman, H. A. Stone, and G. M. Whitesides, "Formation of droplets and bubbles in a microfluidic T-junction scaling and mechanism of break-up," *Lab Chip* **6**(3), 437–446 (2006).
- ¹² A. S. Utada, E. Lorenceau, D. R. Link, P. D. Kaplan, H. A. Stone, and D. A. Weitz, "Monodisperse double emulsions generated from a microcapillary device," *Science* **308**(5721), 537–541 (2005).
- ¹³ S. L. Anna, N. Bontoux, and H. A. Stone, "Formation of dispersions using flow focusing in microchannels," *Appl. Phys. Lett.* **82**(3), 364–366 (2003).
- ¹⁴ S. L. Anna, "Droplets and bubbles in microfluidic devices," *Annu. Rev. Fluid Mech.* **48**, 285–309 (2016).
- ¹⁵ C. Zhou, P. Yue, and J. J. Feng, "Formation of simple and compound drops in microfluidic devices," *Phys. Fluids* **18**(9), 092105 (2006).
- ¹⁶ M. De Menech, P. Garstecki, F. Jousse, and H. A. Stone, "Transition from squeezing to dripping in a microfluidic T-shaped junction," *J. Fluid Mech.* **595**, 141–161 (2008).
- ¹⁷ A. Gupta, H. S. Matharoo, D. Makkar, and R. Kumar, "Droplet formation via squeezing mechanism in a microfluidic flow-focusing device," *Comput. Fluids* **100**, 218–226 (2014).
- ¹⁸ B. Steinhaus, A. Q. Shen, and R. Sureshkumar, "Dynamics of viscoelastic fluid filaments in microfluidic devices," *Phys. Fluids* **19**(7), 073103 (2007).
- ¹⁹ W. Lee, L. M. Walker, and S. L. Anna, "Competition between viscoelasticity and surfactant dynamics in flow focusing microfluidics," *Macromol. Mater. Eng.* **296**(3–4), 203–213 (2011).
- ²⁰ A. Gupta and M. Sbragaglia, "A lattice Boltzmann study of the effects of viscoelasticity on droplet formation in microfluidic cross-junctions," *Eur. Phys. J. E Soft Matter* **39**(1), 1–15 (2016).
- ²¹ J. Husny and J. J. Cooper-White, "The effect of elasticity on drop creation in T-shaped microchannels," *J. Non-Newtonian Fluid Mech.* **137**(1), 121–136 (2006).
- ²² P. E. Arratia, L. A. Cramer, J. P. Gollub, and D. J. Durian, "The effects of polymer molecular weight on filament thinning and drop breakup in microchannels," *New J. Phys.* **11**(11), 115006 (2009).
- ²³ X.-B. Li, F.-C. Li, H. Kinoshita, M. Oishi, and M. Oshima, "Dynamics of viscoelastic fluid droplet under very low interfacial tension in a serpentine T-junction microchannel," *Microfluid. Nanofluid.* **18**(5–6), 1007–1021 (2015).
- ²⁴ L. Derzsi, M. Kasprzyk, J. P. Plog, and P. Garstecki, "Flow focusing with viscoelastic liquids," *Phys. Fluids* **25**(9), 092001 (2013).
- ²⁵ E. Chiarello, L. Derzsi, M. Pierno, G. Mistura, and E. Piccin, "Generation of oil droplets in a non-Newtonian liquid using a microfluidic T-junction," *Micromachines* **6**(12), 1825–1835 (2015).
- ²⁶ T. Fu, L. Wei, C. Zhu, and Y. Ma, "Flow patterns of liquid-liquid two-phase flow in non-Newtonian fluids in rectangular microchannels," *Chem. Eng. Process.* **91**, 114–120 (2015).
- ²⁷ T. Fu, Y. Ma, and H. Z. Li, "Breakup dynamics of slender droplet formation in shear-thinning fluids in flow-focusing devices," *Chem. Eng. Sci.* **144**, 75–86 (2016).
- ²⁸ A. Gupta and M. Sbragaglia, "Effects of viscoelasticity on droplet dynamics and break-up in microfluidic T-junctions: A lattice Boltzmann study," *Eur. Phys. J. E Soft Matter* **39**(1), 1–16 (2016).
- ²⁹ R. B. Bird, P. J. Dotson, and N. L. Johnson, "Polymer solution rheology based on a finitely extensible beadspring chain model," *J. Non-Newtonian Fluid Mech.* **7**(2–3), 213–235 (1980).
- ³⁰ A. Peterlin, "Hydrodynamics of macromolecules in a velocity field with longitudinal gradient," *J. Polym. Sci. B* **4**(4), 287–291 (1966).
- ³¹ D. Izbassarov and M. Muradoglu, "A front-tracking method for computational modeling of viscoelastic two-phase flow systems," *J. Non-Newtonian Fluid Mech.* **223**, 122–140 (2015).
- ³² M. D. Chilcott and J. M. Rallison, "Creeping flow of dilute polymer solutions past cylinders and spheres," *J. Non-Newtonian Fluid Mech.* **29**, 381–432 (1988).
- ³³ S. O. Unverdi and G. Tryggvason, "A front-tracking method for viscous, incompressible, multi-fluid flows," *J. Comput. Phys.* **100**(1), 25–37 (1992).

- ³⁴ G. Tryggvason, B. Bunner, A. Esmaeeli, D. Juric, N. Al-Rawahi, W. Tauber, J. Han, S. Nas, and Y.-J. Jan, "A front-tracking method for the computations of multiphase flow," *J. Comput. Phys.* **169**(2), 708–759 (2001).
- ³⁵ D. Izbassarov and M. Muradoglu, "A computational study of two-phase viscoelastic systems in a capillary tube with a sudden contraction/expansion," *Phys. Fluids* **28**(1), 012110 (2016).
- ³⁶ D. Izbassarov and M. Muradoglu, "Effects of viscoelasticity on drop impact and spreading on a solid surface," *Phys. Rev. Fluids* **1**(2), 023302 (2016).
- ³⁷ S. Homma, K. Moriguchi, T. Kim, and J. Koga, "Computations of compound droplet formation from a co-axial dual nozzle by a three-fluid front-tracking method," *J. Chem. Eng. Jpn.* **47**(2), 195–200 (2014).
- ³⁸ V. Bertola, "Dynamic wetting of dilute polymer solutions: The case of impacting droplets," *Adv. Colloid Interface Sci.* **193**, 1–11 (2013).
- ³⁹ A. Lindner, J. Vermant, and D. Bonn, "How to obtain the elongational viscosity of dilute polymer solutions?," *Physica A* **319**, 125–133 (2003).
- ⁴⁰ H. R. Tamaddon-Jahromi, M. F. Webster, K. Walters *et al.*, "Predicting numerically the large increases in extra pressure drop when Boger fluids flow through," *Nat. Sci.* **2**(1), 1 (2010).